APPLIED RESEARCH

Analysis and Prediction of Temporal and Spatial Evolution of Groundwater Storage by Combined SAR-GRACE Satellite Data

YAN AN[1], FAN YANG[1,2], JIA XU[1], CHUANG REN[1], JIN HU[3], AND GUONA LUO[4]
[1]School of Geomatics, Liaoning Technical University, Fuxin 123000, China
[2]Academy of Science and Technology, Liaoning Technical University, Fuxin 123000, China
[3]POWERCHINA Beijing Engineering Corporation Ltd., Beijing 100000, China
[4]College of Hydraulic and Architectural Engineering, Tarim University, Alar 843300, China

Corresponding author: Guona Luo (1065381600@qq.com)

ABSTRACT Regional surface deformation resulting from the development and utilization of underground space resources poses a significant threat to the safety of urban areas, and the combination of Synthetic Aperture Radar and Gravity Recovery and Climate Experiment (GRACE) satellite data has become a new means to study the impact of underground space evolution on surface deformation. We combine the Interferometric Synthetic Aperture Radar (InSAR) technology and gravity satellite data to extract information on regional surface deformation and groundwater storage changes in Shanxi Province, to explore the patterns of their temporal and spatial variations, to discover their links with seasonal climate change, to re-conceptualize the laws of the regional water cycle, and to quantify the contribution of multiple fields to the evolution of the surface. Furthermore, we propose a novel multi-source neural network prediction model (LSTM/BP) based on signal decomposition (VMD) and algorithm optimization to handle the complex time series characteristics of groundwater storage. Our findings reveal that groundwater storage in Shanxi Province has been consistently declining, with a monthly deficit rate of approximately 1.05 mm. Additionally, there is a notable spatial variation in the annual rate of change, ranging from −21 to 4 mm/year from north to south. Furthermore, we observe a close relationship between inter-annual and seasonal groundwater storage changes and local rainfall patterns, and we find that regional surface deformation is influenced by these groundwater storage changes. The new prediction model outperforms other models, with a root mean square error of 1.56 mm and a correlation coefficient of more than 0.98 on the test set. The model improves the prediction accuracy of the groundwater reserves in the basin, and it can be used to provide a reference for the comprehensive management of the groundwater in Shanxi Province, the rational development of mineral resources, and other major national needs.

INDEX TERMS GRACE, InSAR, groundwater storage, surface deformation, VMD, LSTM.

I. INTRODUCTION

For human production and survival, groundwater is an indispensable resource, which affects socioeconomic development and ecological balance, and plays an important role in safeguarding the life of residents and resource allocation. groundwater storage (GWS), as an important indicator of

The associate editor coordinating the review of this manuscript and approving it for publication was Tai Fei.

regional water resource changes, is of great significance to explore the characteristics and distribution of its spatial and temporal changes, and to understand how the basin's water resources are protected and developed in an environmentally friendly manner [1], [2]. However, due to the complexity and difficulty of observing groundwater, the development and management of groundwater resources have been facing many challenges [3], [4], [5].

Traditional groundwater monitoring methods have limitations due to high cost, low accuracy, inconsistent scale, and difficult interpretation [6]. The release of Gravity Recovery and Climate Experiment (GRACE) gravity satellites has enabled large-scale monitoring of terrestrial water storage (TWS). Monitoring the Earth's gravity field allows GRACE to invert changes in mass distributions, which in turn yields changes in TWS [7], [8]. Since then, a new groundwater inversion method has been proposed, which combines the water balance equations and hydrological modeling, to separate information on changes in GWS from changes in TWS [9], [10], [11], [12]. Domestic and foreign experts and scholars in many fields have achieved remarkable results in inverting the change of TWS and GWS using GRACE data. These include revealing the water system changes in the Amazon and Songhua River basins [13], [14], exploring the groundwater flow trends in the land plains [15], analyzing the local hydroclimatic characteristics [16], [17], and combining radar data, such as Sentinel data, to carry out correlation studies of groundwater and surface deformation [18], [19], [20].

Various geodetic techniques are used to measure deformations on a range of temporal and spatial scales. Geodetic leveling provides highly accurate discrete point data over a localized area by comparing the height difference between two points. However, most of the monitoring of such hydrologically induced surface deformation over time is carried out on limited spatial and temporal scales. In recent years, there has been an increase in the application of Interferometric Synthetic Aperture Radar (InSAR) as a remote sensing technique for millimeter-scale ground subsidence mapping. Satellite-based methods have some advantages in measuring land deformation because of the low cost of obtaining processed data and the fact that the results can provide more details about the spatial scattering of land deformation areas. With the gradual development of InSAR technology, geodetic observations provide useful data to understand the processes occurring at greater depths of deformation, and the deformation time series derived from InSAR is not only used to map the spatial distribution of ground subsidence in aquifer systems but can also be used to estimate the water storage coefficients of aquifers and to predict changes in aquifer head [21], [22], [23]. Thus, InSAR provides a new tool to characterize the storage properties of aquifer systems, the boundaries of confined aquifers, and settlement characteristics in time and space.

Research in the field of Earth sciences is increasingly dependent on remote sensing technologies and satellite data, and the continuous development of these technologies has provided us with more tools to understand the complexity of the Earth system. Among them, the study of techniques combining InSAR and GRACE has become a hot research topic in the fields of groundwater and surface deformation. With InSAR technology, surface subsidence or uplift can be monitored, while GRACE data provides the overall trend of groundwater storage. By combining these two types of data,

researchers can more accurately assess groundwater changes, identify increases or decreases in groundwater storage, and explore the effects of groundwater changes on surface deformation. Li et al. analyzed the surface deformation induced by groundwater in the North China Plain by using the InSAR-GRACE technique, and explored the coupling relationship between groundwater-surface deformation [24]. Gong et al. also proposed the risk warning and safety outlook of urban underground space under the new groundwater environment, and they believed that combining with the InSAR-GRACE technology, they could build a research framework of the surface response of the underground space evolution and reveal the formation mechanism of the surface subsidence response pattern, so as to establish an emerging risk prevention and control warning mechanism for the safety of underground space and realize the scientific regulation of the region [18].

Since the release of gravity satellite data, there has been an increasing number of studies combining multi-source data to invert and analyze changes in groundwater storage and their influencing factors, but there have been few studies related to time-series prediction of groundwater storage. Part of the reason is that GWS changes are affected by multiple natural factors such as precipitation and evaporation, and traditional groundwater prediction models rely on complex hydrologic and geologic information [25], [26]. Meanwhile, traditional prediction models such as Autoregressive (AR) and gray prediction models have limited accuracy in predicting GWS due to their linear nature [27]. In the era of computer technology, the emergence of intelligent algorithms based on machine learning has improved the reliability of GWS prediction. Literature [28] verified the feasibility of GWS prediction by GRACE satellite using an approach, i.e., Support Vector Machine (SVM); literature [29] successfully predicted GWS in distinctive types of aquifers by using Nonlinear Autoregressive Networks with Exogenous Input (NARX) with rainfall and temperature as driving factors. Although neural networks can improve the accuracy of GWS prediction, different network types and structures have different prediction performances, and the time series characteristics of GWS changes are complex, so it is difficult to rely on a single neural network structure to effectively analyze and discriminate. According to the idea of signal decomposition decomposing the complex signal features into components with certain physical significance is a feasible solution, and by applying each component to a suitable neural network structure, the trend of each component in the future can be effectively predicted, and then the change of the original signal features can be restored.

In this paper, from the inversion of regional GWS, the missing data in GRACE gravity satellite data are filled in by Singular Spectrum Analysis (SSAN) [30], and based on the complete sequence of GRACE data, the simultaneous Global Land Data Assimilation System (GLDAS) is combined to invert the TWS and GWS in Shanxi Province from 2002 to 2022. The spatial distribution characteristics and time-series changes of GWS and precipitation

are analyzed to explain the relationship between GWS and precipitation during these 20 years. Combined with Sentinel-1 satellite data, Small Baseline Subset Interferometric Synthetic Aperture Radar (SBAS-InSAR) technology is used to focus on extracting deformation characteristics of areas with serious changes in GWS, and the correlation between the two is studied through the surface-groundwater coupling model. Finally, a multi-source neural network prediction model based on signal decomposition and algorithm optimization is proposed for the complex time-series characteristics of GWS, and the reasonableness of the model is verified through the evaluation indexes, and a reasonable prediction is made for the future changes of GWS in the study area. To provide a gauge for the comprehensive governance of groundwater in Shanxi Province, rational development of mineral resources, and other major national needs.

II. STUDY AREA

Shanxi Province is located in North China, geographically between longitude 110°14′ 23″ and 114°33′ 20″ East and latitude 34°34′ 11″ and 40°44′ 38″ North, bordering several provinces and autonomous regions. Located in the upper reaches of the Yellow River, Shanxi Province is a typical mountainous plateau covered by loess. Westward is a high terrain, while eastward is a low terrain, with river valleys running across, and is mainly composed of mountains, hills, and other landforms. Among them, the Taihang Mountains and the Luliang Mountains run through the whole territory of Shanxi Province, forming the main geographical features of Shanxi. Geologically, Shanxi Province is an important mineral resource area, with abundant coal, iron, copper, and other mineral resources. This has an important impact on China's economic, cultural, and social development.

Shanxi Province is located in the interior of the mid-latitude zone and has a temperate continental monsoon climate in terms of climate type. The annual precipitation in all parts of the province ranges between 400-700 millimeters, with uneven seasonal distribution, and the precipitation is relatively concentrated in the summer months of June-August, accounting for about 60% of the annual precipitation, and the distribution of precipitation in the province is greatly influenced by the topography. Shanxi Province is the watershed of the two major basins of the Yellow River and the Haihe River, the province's Yellow River basin covers an area of 97,138 square kilometers, accounting for 62.2% of the province's area, and the Haihe River basin covers an area of 59,133 square kilometers, accounting for 37.8% of the province's area. In addition to the mainstream of the Yellow River, which flows through the west and south of the provincial border for 965 kilometers, there are five larger rivers in the province with a watershed area of more than 10,000 square kilometers, namely, the Fen River and the Qin River in the Yellow River Basin, and the Sanggan River, the Zhang River and the Hutuo River in the Hai River Basin. Rivers in Shanxi Province are self-produced outflow-type water systems, with
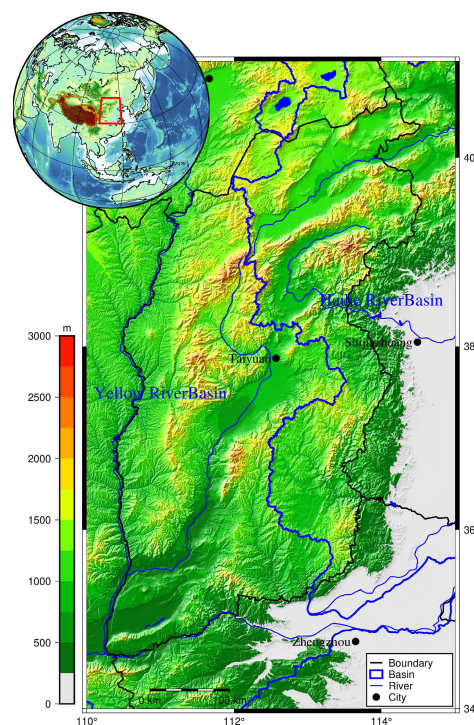

FIGURE 1. Geographic location and geology of shanxi province.

river water coming from atmospheric precipitation, most of them originating in the territory and dispersing outflow to the outside of the province. Due to this, it is important to study the characteristics of GWS changes in Shanxi Province to understand the optimal allocation of water resources on a large scale across basins.

Shanxi Province is rich in groundwater resources and plays an important role in local agricultural, industrial, and domestic water use. The depth of the water table and the tectonic characteristics of the aquifers in Shanxi Province vary in different regions. Generally speaking, the groundwater table in Shanxi Province is relatively shallow, mostly distributed in the range of 10-50 meters below the surface. However, in some areas, the groundwater level may decline due to excessive groundwater exploitation or insufficient groundwater recharge [31]. Groundwater in Shanxi Province mainly comes from precipitation infiltration and vadose flow and is mainly divided into two types: shallow groundwater and deep groundwater. Shallow groundwater is mostly distributed in river valleys, lakes, and plains, and the aquifers are usually gravel, sand, and gravel, or sandy soils; deep groundwater is mostly distributed in mountainous areas and pre-mountain plains, and the aquifers are mostly water in rock fissures [32]. In general, groundwater resources in Shanxi Province are one of the important water sources in the region, and reasonable management and protection of groundwater resources are of great significance in realizing sustainable development and safeguarding the benign cycle of people's life and ecological environment. The geographic location and geological structure of Shanxi Province are shown in Figure 1.

**TABLE 1.** Tyres of data and their related information.

Type of data	Datasets	Time distribution	Time resolution	Spatial resolution	Source
Satellite gravity data	GRACE_RL06_Mascons	2002.4-2022.12	Month	0.25°×0.25°	CSR（https://www2.csr.utexas.edu/grace/）
hydrological model	GLDAS_NOAH_v2.1	2002.4-2022.12	Month	0.25°×0.25°	GESDISC(https://disc.gsfc.nasa.gov/)
Precipitation data	TRMM_3B43	2002.1-2019.12	Month	0.25°×0.25°	GESDISC(https://disc.gsfc.nasa.gov/)
Radar data	Sentinel-1A	2021.1-2021.12	12day	5×20m	ESA（https://scihub.copernicus.eu/dhus/#/home）
DEM data	SRTM1	—	—	30×30m	NASA（https://www.earthdata.nasa.gov/）

III. MATERIALS

GRACE gravity satellite data and GLDAS hydrological data are the basic data for the inversion of regional GWS. To further study and analyze the factors that cause changes in GWS and the impact of GWS changes on surface deformation, other hydrological data and radar data for observing surface deformation are also applied in this paper. Detailed information on the data is shown in Table 1.

A. GRACE GRAVITY SATELLITE DATA

The GRACE gravity satellite is a satellite developed by the National Aeronautics and Space Administration (NASA) in cooperation with the German Space Center (GFZ) to observe changes in the Earth's gravity field. By providing a high-precision time-varying gravity field, it is possible to infer the change and distribution of the mass of the Earth's surface [33]. The GRACE gravity model has two product forms, the Spherical Harmonics (SH) and the Mascons, and the traditional SH data have become an important factor limiting its development due to the cumbersome processing and the low spatial resolution. The emergence of Mascons products effectively overcomes the shortcomings of SH products, taking into account the removal of north-south strip error noise and the correction of leakage errors, while at the same time improving the spatial resolution of the product, so that there is a better delineation of land and sea boundaries. In this paper, we use the RL06_Mascons product released by the Center for Space Research (CSR) of the University of Texas, USA, with a spatial resolution of 0.25°, and a total of 216 periods of data from April 2002 to December 2022 in cm, changes in total TWS expressed as equivalent water heights. Due to the missing data in some months, the vacant data were interpolated using SSAN. The SSAN interpolation method for missing values is to utilize the temporal correlation of the available samples to deal with the time series of the missing samples. Nico added two loops based on the original SSAN idea and updated the missing values by iterating to gradually increase the reconstruction complexity until the hypothetical value tends to be the optimal one [30]. The interpolated time series are shown in Figure 2, with gray dots representing the original data, red dots representing the interpolated CRACE satellite data, and blue dots representing the interpolated GRACE-
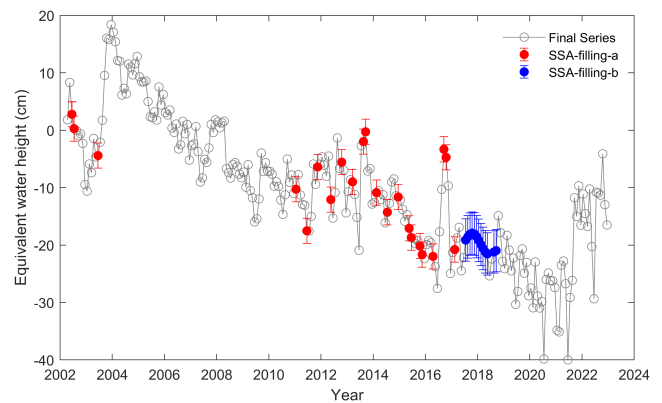
FIGURE 2. Time series of GRACE data after applying the SSAN interpolation method.

Follow on(GRACE-FO) satellite data, as well as data between GRACE and GRACE-FO satellites.

B. GLDAS HYDROLOGIC MODEL DATA

The GLDAS, jointly constructed by NASA and the National Centers of Environmental Prediction (NCEP), is a high-resolution global land hydrological simulation system. It provides high-resolution, near-real-time surface state information by assimilating ground and satellite observations [12]. GLDAS provides four model products that contain a variety of surface hydrologic data such as soil moisture (SM), plant canopy surface water (PW), snow depth water equivalent (SWE), and storm surface runoff (QS). In this paper, the NOAH version is selected, and the spatial and temporal resolution is consistent with the GRACE data, with a total of 249 periods of data. Since the background value deducted from the CSR_Mascons data is the average value from January 2004 to December 2009, therefore, the GLDAS data were de-averaged during data processing (Surface water month by month minus its average from January 2004 to December 2009).

C. OTHER DATA

The Tropical Rainfall Measuring Mission (TRMM) provides precipitation datasets covering latitudes 50°S-50°N [34].

In this paper, TRMM_3B43 data were selected with a spatial resolution of 0.25° ∼0.25°, with a temporal distribution from January 2002 to December 2019, totaling 18 years and 216 months. The data are in mm/hr, and the text is converted to monthly and annual scales for analysis. Sentinel-1, a geohazard monitoring satellite constructed as part of the European Space Agency's (ESA) Copernicus Earth Observation Program, was launched in 2014 and has begun continuous observation of the Earth's progression [35]. Sentinel-1A data was selected as the main data source for InSAR monitoring, and a total of 24 images covering the study area were acquired, with a time range between January 2021 and January 2023, and a revisit period of about 30 days. In the process of InSAR data interpretation, external Digital Elevation Model (DEM) data used to simulate and remove the terrain phase is essential [36]. According to the research of Lu et al. [37] the participation of Shuttle Radar Topography Mission (SRTM1) data in the area with large terrain undulation can be interpreted to produce better deformation results, so in the case of the same resolution, this paper selects the SRTM1 with higher accuracy as the reference DEM data.

IV. METHODS

A. DESEGREGATION OF TWS

The TWS changes in the GRACE data inversion include surface water storage (SWS) changes and GWS changes, and the SWS mainly consists of SM, PW, SWE, and QS, etc, which is negligible considering that the amount of QS changes in the study area is small. The change in GWS can be obtained by deducting the change in SM, PW, and SWE from the change in TWS based on the desegregation of TWS [7]. Previous studies have also estimated GWS from GRACE data using a similar methodology, i.e.:

$$\Delta GWS = \Delta TWS - \Delta SM - \Delta PW - \Delta SWE \quad (1)$$

where ΔGWS represents the change in groundwater storage, ΔTWS represents the change in terrestrial water storage, and ΔSM, ΔPW, and ΔSWE are the changes in soil water, vegetation water, and snow water, respectively. The processing flow is shown in STEP ONE of Figure 3.

B. SBAS-InSAR PROCESSING

The SBAS-InSAR technique was first proposed by Berardino et al [38], [39], [40] and the basic idea is to obtain the same Multiple SAR images of a region are selected and pixels that meet certain conditions on these images are selected for time series analysis. Compared with other time-series InSAR techniques, the SBAS-InSAR technique is unique in that it requires the processing of multiple interferometric pairs, and the temporal and spatial baselines of the interferometric pairs need to be kept within a certain threshold range at the same time, and the interferometric pairs are subjected to multi-visualization in phase space, which reduces the spatial
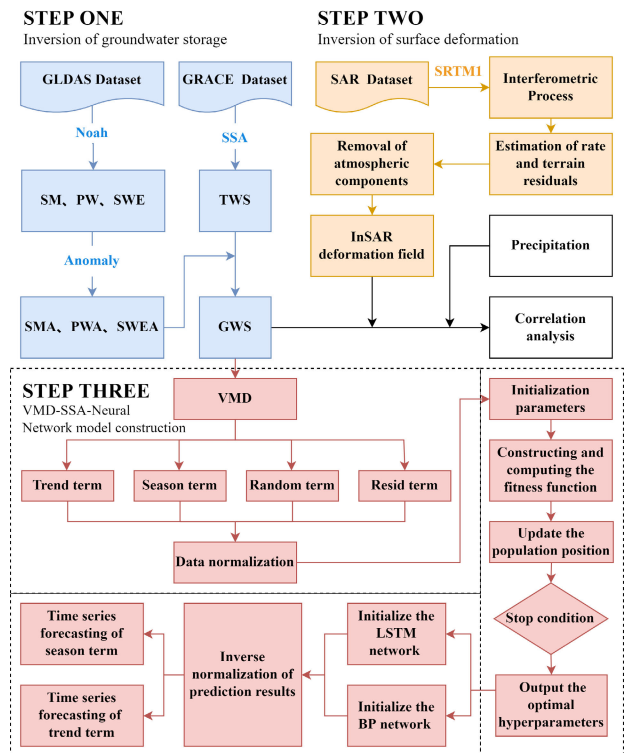

FIGURE 3. Flow chart of GWS inversion and prediction.

resolution of the image but also ensures the maximum coherence of the interferometric phase. The basic principles of the SBAS-InSAR technology are not repeated in this paper, see STEP TWO of Figure 3.

C. MULTI-SOURCE NEURAL NETWORK MODELING

1) VARIATIONAL MODE DECOMPOSITION

Variational Mode Decomposition (VMD) was proposed by Dragomiretskiy and Zosso in 2014 [41]. Its advantage lies in its ability to determine the number of decomposed modes according to different situations, and to adapt and match the decomposition of the intrinsic modal components according to the optimal center frequency and finite bandwidth of each mode. Compared with other decomposition algorithms, VMD overcomes the problems of modal aliasing and endpoint effects and reduces the non-stationarity of complex and non-linear time series. The main step is to construct a solution to the variational problem:

$$\begin{cases} \min_{\{u_k\},\{\omega_k\}} \left\{ \sum_k \left\| \partial_t \left[\left(\delta(t) + \frac{j}{\pi t} \right) * u_k(t) \right] e^{-j\omega_k t} \right\|_2^2 \right\} \\ \text{s.t.} \sum_k u_k = f(t) \end{cases}$$

$$(2)$$

where: k-number of decomposed modes; u_k-decomposition of the resulting k modal components; ω_k-center frequency; $*$-convolution operation; $f(t)$-original signal; ∂_t-gradient operation.

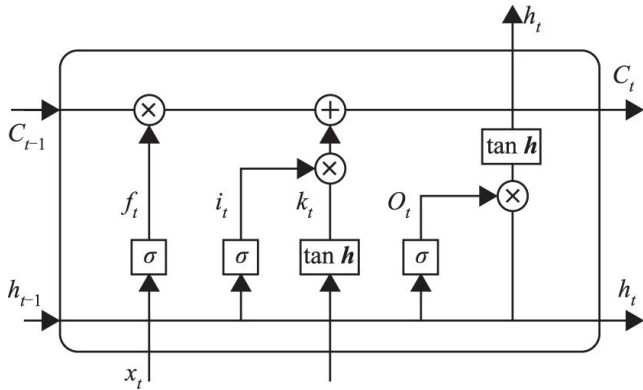**FIGURE 4.** Basic LSTM model structure.

2) SPARROW SEARCH ALGORITHM

Sparrow Search Algorithm (SSA) is inspired by the mechanism of sparrow's foraging behavior and predator avoidance behavior [42]. Sparrow algorithm has the advantages of high optimality finding ability and fast convergence speed. Each sparrow represents a location attribute i.e. where it finds food. Each sparrow plays three different roles in the global scenario: the finder, which searches for food within a certain range; the joiner, which follows the finder to find the best food; and the alert, which is alert to the surrounding dangers and warns when it senses danger. The main steps are shown in STEP THREE of Figure 3.

3) LONG SHORT-TERM MEMORY NEURAL NETWORKS

Long Short-Term Memory (LSTM) is a streaming variant of the traditional Recurrent Neural Network (RNN), first proposed by Hochreiter and Schmidhuber [43], [44]. The LSTM has two main modules that help it learn temporal characteristics from data. The first is the memory module, which is used as the cell state. The second is the gate module, an input gate, an output gate, and an oblivion gate, which effectively trains the fully connected layer to control the cell state in response to new inputs from the data and past outputs of the model. The main principle is shown in Figure 4.

4) BACK PROPAGATION NEURAL NETWORKS

The Back Propagation (BP) neural network, initially introduced by a scientific team led by Rumelhart and McClelland in 1986, comprises three components: the input layer, hidden layer, and output layer. The basic principle is that the external information through the input layer neurons into the BP network, through the design of one or more hidden layers of the intermediate layer, the input information is processed and transformed, by the last hidden layer of the processed information will be transmitted to the output layer neurons, to complete the propagation of a positive learning process. After further processing, the result of the information learning process is transmitted from the output layer, and when the output fails to meet the desired specifications, it undergoes the reverse propagation process of the error.

5) BUILDING VMD-SSA-LSTM/BP NEURAL NETWORK PREDICTION MODEL

Combining the VMD technique, SSA, and LSTM and BP neural network models, the VMD-SSA-LSTM/BP neural network prediction model is constructed, as shown in STEP THREE of Figure 3, and the model implementation process is as follows:

The original time series data $X(t)$ to be predicted is subjected to VMD signal decomposition to obtain n components $IMF_i(t)$ and residual $Re(t)$. The formula is as follows:

$$X(t) = \sum_{i=1}^{n} IMF_i(t) + Re(t) \tag{3}$$

Establish the SSA-LSTM model and SSA-BP model for the obtained n components and residuals, respectively, and use SSA to find the optimal hyperparameters in LSTM and BP models

The obtained optimal hyperparameters are applied to the LSTM and BP neural networks to initialize the training and prediction in the form of components.

The predicted values of the components are superimposed to obtain the predicted values of the original data and error analysis is performed.

Multi-step prediction of future values based on existing data. Assuming that the data $Y(t) = \{y_1, y_2, \ldots, y_n\}$ is known and to predict the future k steps, there are:

$$y_{n+i} = M(Y(t)) \ (i = 1, \ldots, k) \tag{4}$$

where M represents the prediction model, assuming k > 2. Then the first predicted value $y_{n+1} = M(\{y_1, y_2, \ldots, y_n\})$, Afterwards update the known data $Y(t)$, Putting y_{n+1} into the model, that is $y_{n+2} = M(\{y_2, \ldots, y_n, y_{n+1}\})$, and so on until after looping k times, the predicted value $Y'(t) = \{y_{n+1}, y_{n+2}, \ldots, y_{n+k}\}$ is obtained.

D. EVALUATION METRICS

To evaluate the reliability of the model during the experiment, the Pearson correlation coefficient (R), Root Mean Square Error (RMSE), Mean Square Error (MAE), and Mean Absolute Percentage Error (MAPE) to evaluate the prediction accuracy of the model. Among them, R is used to judge the predictive ability of the model, and the closer the value is to 1, the better the correlation between the observed and predicted values; RMSE is used to measure the global fit of the prediction model, and the smaller the value is, the better the consistency of the data is; MAPE is used to evaluate the accuracy of the predicted data, and the smaller the percentage of the value is, the higher the accuracy of the predicted data is. Their formulas are as follows:

$$R = \frac{\sum_{t=1}^{n} (y_t - \hat{y})(\bar{y}_t - \hat{\bar{y}})}{\sqrt{\sum_{t=1}^{n} (y_t - \hat{y})^2} \sqrt{\sum_{t=1}^{n} (\bar{y}_t - \hat{\bar{y}})^2}} \tag{5}$$

$$RMSE = \sqrt{\frac{\sum_{t=1}^{N} (y_t - \bar{y}_t)^2}{N}} \tag{6}$$

$$\text{MAE} = \frac{1}{N} \sum_{t=1}^{N} |y_t - \bar{y}_t| \tag{7}$$

$$\text{MAPE} = \frac{100\%}{N} \sum_{i=1}^{N} \left| \frac{y_t - \bar{y}_t}{y_t} \right| \tag{8}$$

where y_t and $\bar{y}_t$ denote the observed and predicted values of the data at moment t, respectively, $\hat{y}$ and $\hat{\bar{y}}$ represent the means of the actual observations and model predictions, respectively, and N is the total number of sample test sets.

V. CHANGES IN GROUNDWATER STORAGE AND ANALYSIS

A. TIME SERIES CHANGES

The SSAN method was first used to fill in the missing GRACE data, while the SM, PW, and SWE data from the NOAH version of the GLDAS hydrological model were extracted and de-averaged to obtain the SMA, PWA, and SWEA data. Finally, according to the principle of water balance, the time series change of GWS in the study area is obtained by inversion of joint GRACE and GLDAS data, as shown in Figure 5, in which the blue hollow point indicates the real value of storage obtained by inversion, the red curve indicates the time series change of storage, and the black dotted line indicates the time series of change of storage after the least squares linear fitting. It can be seen that from 2002 to the end of 2022, the change of TWS shows an overall decreasing trend, with an average trend of -9.1 mm/a. Starting from April 2002, the change of TWS first shows an increasing trend and reaches the maximum value of 183.8 mm in December 2003, which indicates that the TWS within Shanxi Province is in a state of maximum surplus at this time. After that, it showed a continuous downward trend, and the minimum value of -399.9 mm appeared in April 2021, at which time the TWS was in the state of maximum deficit. According to Figures a and c, it can be seen that the change of GWS and the change of TWS have the same trend of change, and the periodic fluctuation is also consistent, with an average trend of change of -10.3mm/a. According to Figure d, the two have a strong correlation, with the Pearson correlation coefficient of 0.98, which indicates that the change of TWS within the study area is mainly caused by the change of GWS. Changes in SWS, such as soil water, have little effect on it. Changes in SWS are relatively stable, but there are some cyclical changes, with the largest surplus occurring in April 2003 and the largest deficit occurring in September 2006.

Figure 6 reflects the segmented trend of GWS change, from which it can be seen more clearly that the change of GWS an upward, then downward, then upward trend, showing different states in different periods, and the rate of change is large. Since April 2002, the GWS has been rising at an average rate of 11.4 mm/month, reaching a peak of 175.7 mm in July 2003, when the GWS is in maximum surplus. From August 2003 to April 2021, the GWS continued to be in deficit at a faster rate, with a deficit rate of 1.9 mm/month. the minimum value of -396.3 mm occurs in April 2021, when the GWS

is in maximum deficit. Overall, the GWS in the study area is highly variable during these 20 years, fluctuating periodically between -400 to 200mm and is in deficit for a long period, Groundwater storage begins to rebound at a faster rate until the second half of 2021.

B. SPATIAL DISTRIBUTION CHARACTERISTICS

Figures 7 and 8 show the annual rate of change and spatial distribution of GWS in the study area during 2003-2022, respectively. As shown in Figure 7, the annual rate of change of GWS in most areas of Shanxi Province is negative, implying that GWS is decreasing, and only the annual rate of change in Yuncheng City in the southernmost part of Shanxi Province is positive, and GWS shows an increasing state. The spatial difference of GWS varies significantly, with the annual rate of change fluctuating from -21 to 4 mm/a, which is consistent with the spatial distribution of local precipitation. In the region with more precipitation, the rate of change of GWS is slower, and in the northern cities with less precipitation, the annual rate of change of GWS is relatively larger.

From Figure 8, the spatial variation of GWS in Shanxi Province is obvious, and there is a significant inter-annual variation characteristic. It can be seen that the spatial distribution of GWS between 2003 and 2006 varied somewhat, but the overall change was relatively stable, with all pixels remaining around 0 mm. GWS began to decline at a certain rate after 2007, and GWS in the eastern part of the river, bounded by the middle reaches of the Fen River in the study area, continued to decrease in a deficit state and gradually moved northward spatially over time. This may be due to the movement of rock layers and the surface caused by the exploitation of underground resources, which in turn generates water-flowing fractured zones that open up the connection between the groundwater and the surface, allowing large quantities of groundwater to pour into the surface [45], [46]. After 2014, the rate of decline in GWS increases, and spatially, the deficit state starts in the southeast corner of Shanxi Province and moves northwestward, with the largest areas of deficit occurring in Changzhi and Jinzhong cities. Until 2022 GWS shows a substantial recovery, keeping the average value of groundwater storage around -280 mm. Only Yuncheng City in the south of the whole study area maintains a continuous growth of GWS, with a maximum growth rate of up to 4 mm/a. By comparing the spatial distribution of rainfall in Figure 9, there is a strong consistency between them, which is probably affected by the climatic conditions.

C. THE RELATIONSHIP WITH PRECIPITATION CHANGES

To study the relationship between GWS and local precipitation, the monthly average precipitation, annual average precipitation, and its spatial distribution in Shanxi Province from 2002 to 2019 were counted, as shown in Figures 9a and 10a. The study area is bounded by Taiyuan, the provincial capital and the precipitation is larger in the southeast, with Yuncheng, the southernmost city, being the city with the
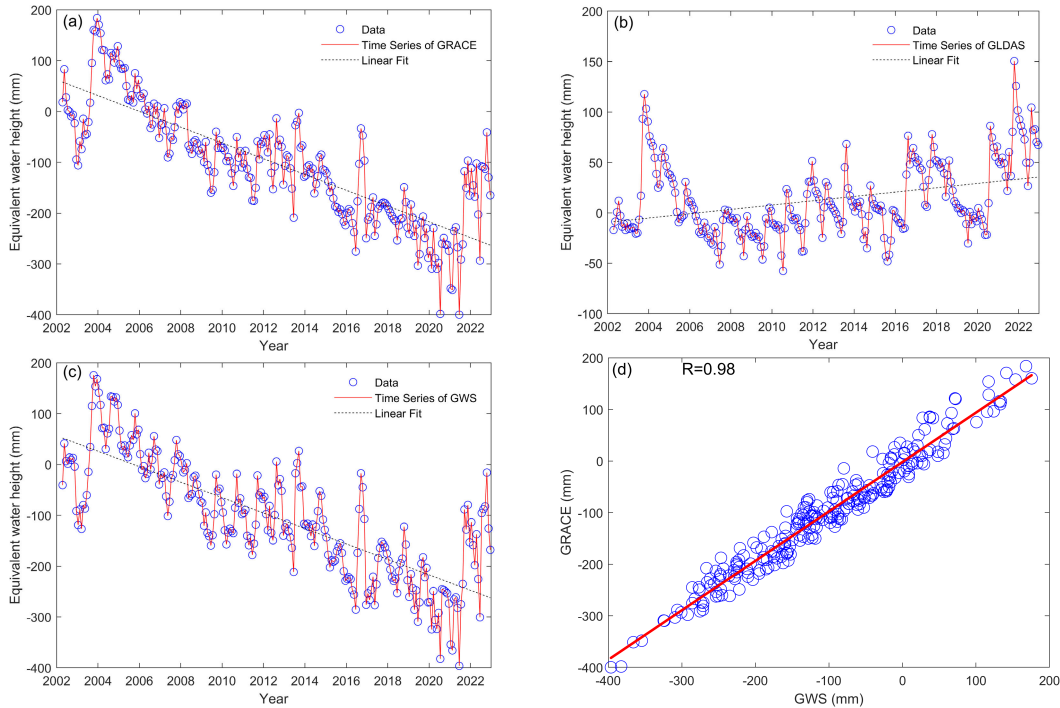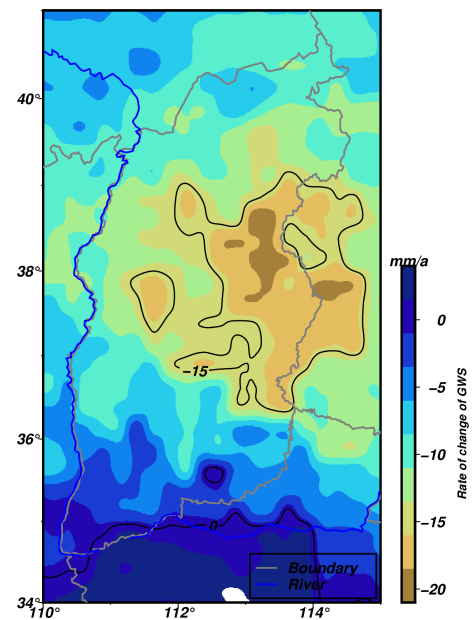
FIGURE 5. The curve of change in (a) TWS, (b)SWS, and (c) GWS in the study area from 2002 to 2022, and (d) Correlation curves of GWS and TWS.(The blue hollow point indicates the real value of water storage obtained by inversion, the red curve indicates the time series change of water storage, and the black dotted line indicates the time series of water storage change after least squares linear fitting.
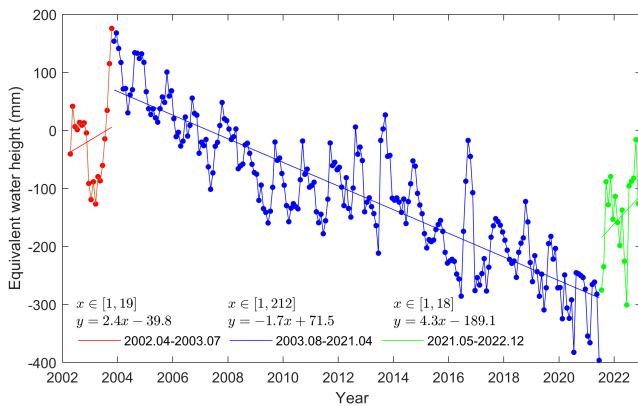
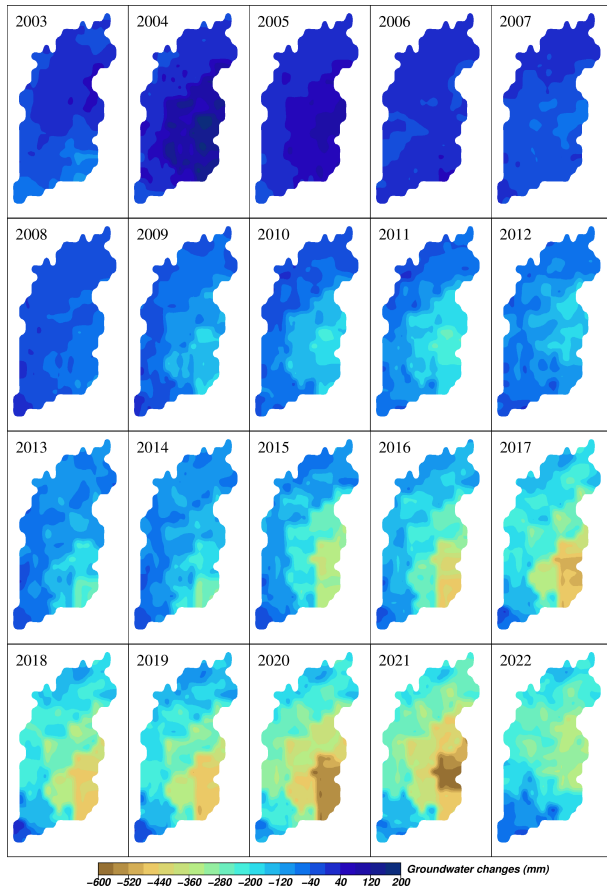**FIGURE 6.** Segmented time series of GWS changes in the study area, 2004-2022.

FIGURE 7. Annual rate of change in GWS in the study area, 2003-2022.

largest precipitation in Shanxi Province, with a maximum of up to 736 mm/a, the precipitation in the northwest is relatively small, with a minimum of 434 mm/a, and it is located in Datong, the northernmost city in Shanxi Province. It can be seen that for the north-south-oriented study area, the southern cities can receive more precipitation recharge to mitigate the effects of a significant GWS deficit. The northern cities, on the other hand, can only rely on artificial forms of GWS replenishment, such as ecological water conveyance, when precipitation is insufficient.
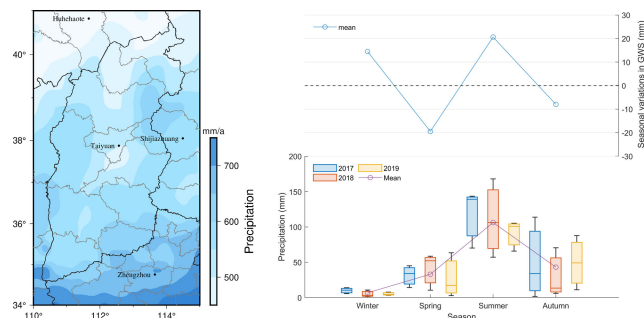
In terms of temporal distribution, the time series is relatively flat with little difference in precipitation except for a few years when precipitation is relatively high. A comparison of the patterns of average monthly precipitation and GWS changes reveals that when monthly precipitation reaches its
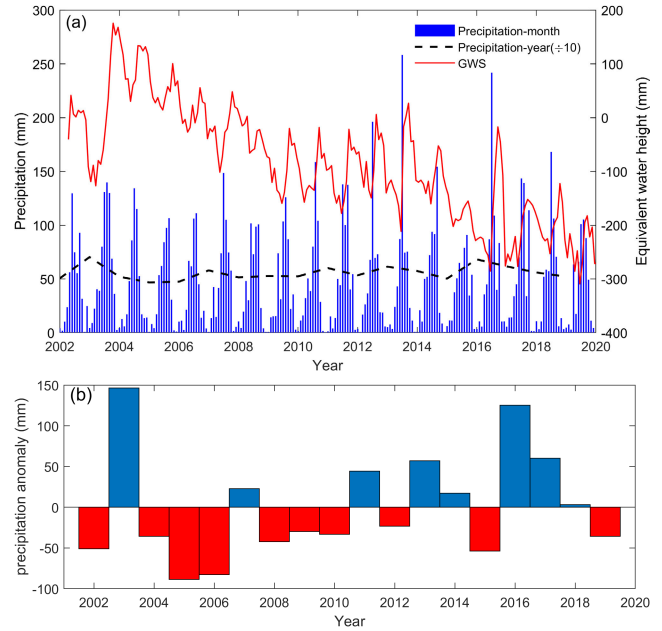
FIGURE 8. Spatial distribution of GWS changes in the study area, 2003-2022.

FIGURE 9. Spatial distribution and seasonal variation of precipitation (a) Characteristics of the spatial distribution of mean annual precipitation and (b) Variation of precipitation in different seasons from 2017-2019.

FIGURE 10. (a) Monthly and annual mean precipitation data and (b) Annual mean precipitation anomalies in the study area from 2002 to 2020. (Dark blue rectangles represent average monthly precipitation and black dashed lines represent average annual precipitation).

and the larger the value, the higher the precipitation. By comparing the changes in GWS and precipitation anomalies in the study area, it can be found that the change pattern of GWS is consistent with the characteristics of the changes in average annual precipitation. The years from 2004 to 2010, when precipitation was 10-100 mm lower than the average value and GWS declined sharply, and the years when GWS showed a rapid rebound coincided with an increase in precipitation during the same period. In years with high precipitation (precipitation anomaly is positive), farmland crops get more supply from precipitation, the demand for irrigation is reduced, and the amount of groundwater extraction is also reduced, while the increased precipitation recharges the groundwater, slowing down the decline in groundwater reserves caused by extraction; in years with low precipitation (negative precipitation anomalies), the source of groundwater recharge decreases while the demand for extracted groundwater from irrigation of agricultural fields increases, further exacerbating the groundwater deficit in the basin. For the study area, excessive groundwater resource extraction has resulted in stable precipitation that can no longer meet supply requirements, plus the study area is located in central China and lacks additional groundwater recharge from glaciers and other sources, resulting in a continued decline in GWS.

The changing pattern of GWS and precipitation with the change of seasons is further analyzed in Figure 9b. Normally, March-May represents spring, June-August represents summer, September-November represents fall, and December-February represents winter [47]. The time series of GWS is processed using Fourier spectral analysis to obtain

peak, the GWS change also reaches its highest point, indicating that precipitation is very important for the supply of GWS. Figure 10b represents the average annual precipitation anomalies in the study area, obtained by de-averaging the average precipitation for each year one by one. Negative values indicate that the precipitation for the year is lower than the multi-year average, and larger values represent lower precipitation. Positive values, on the other hand, indicate that the annual precipitation is higher than the multi-year average,

its spectral distribution and change rule. The precipitation data from 2017-2019 were taken, grouped, and statistically averaged according to different years and seasons. It can be seen that the changes in GWS and precipitation in the study area during the four seasons have a clear distribution pattern, and the trends are relatively close to each other. Among them, the change in GWS was negative in spring, when GWS was in maximum deficit. The change in GWS turned positive in summer, when GWS was in maximum surplus, due to the increase in precipitation in summer, which resulted in the replenishment of groundwater by surface runoff. In the fall period, the GWS was in deficit again, but the groundwater consumption was reduced compared with that in spring, possible reasons for this are the rapid decrease in precipitation and higher evaporation due to the still high temperatures in the fall. The change in GWS is not much different between winter and summer, indicating that the consumption of GWS in winter is less than in summer in the presence of small amounts of precipitation.

### D. THE RELATIONSHIP WITH REGIONAL SURFACE DEFORMATION

PIE series products are based on a fully loosely coupled underlying architectural design, with flexible and scalable architecture. PIE-SAR is a satellite-mounted SAR data processing and analysis software, which provides a graphical interface to support the data processing and analysis of domestic and foreign mainstream satellite-mounted SAR sensors. In this paper, Sentinel-1 data are preprocessed by PIE-SAR, including data import, image cropping, geocoding, and so on.

Taiyuan City and Yuncheng City, which have large annual change rates of GWS, were selected as the key areas for extracting surface deformation features, and the SAR images covering Taiyuan City and Yuncheng City were pre-processed and decoded respectively. To obtain interferometric pairs with higher coherence, the maximum temporal baseline was set to 150 and 100 days, respectively, and the maximum spatial baseline to 10% of the critical baseline [48], [49]. The spatial baseline connectivity of the image pairs is shown in Figure 11, where the X-axis represents the date, the Y-axis represents the baseline distance between the two view images, and the red and green dots represent the distribution of the primary and secondary images on the time series, respectively.

The orbit information is corrected using AUX_POEORB satellite precision orbit data to remove the systematic errors caused by the orbit information, the terrain phasing is eliminated by using STRM1 data. Atmospheric delay errors are corrected or removed using GACOS water vapor data. In addition, the azimuth looks and range looks were set to 4 and 1, and the grid size for suggested looks was set to 50 m. A Goldstein filter was used to remove the noise phase, and the filtered interferogram was phase-disentangled using the minimum cost flow (MCF) method, The time series deformation is then inverted by singular value decomposition.
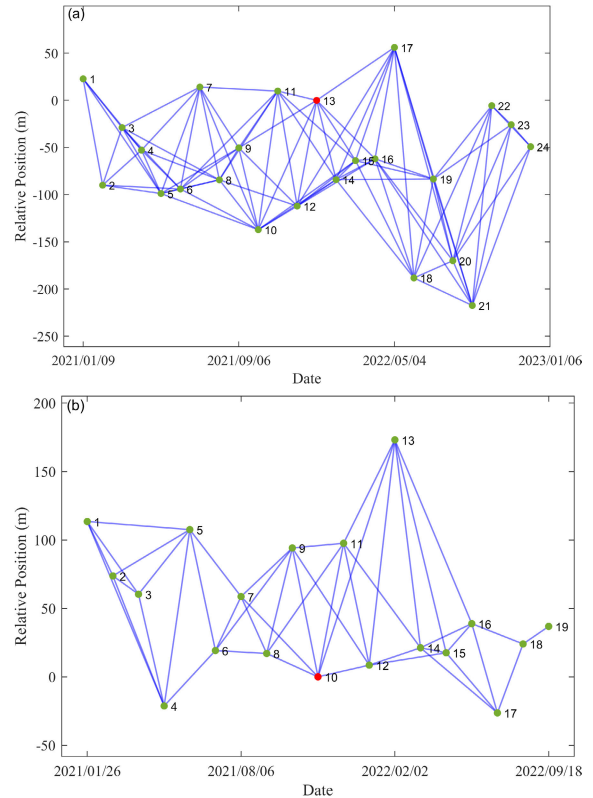

FIGURE 11. Spatial baseline connectivity diagram (a) Taiyuan City and (b) Yuncheng City.
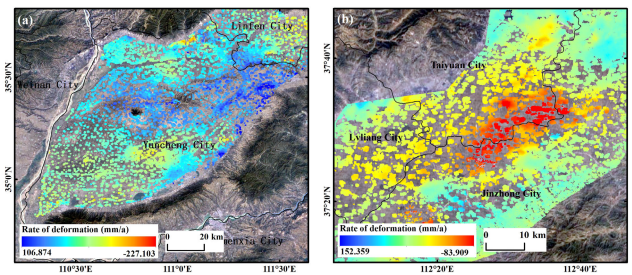
FIGURE 12. Spatial distribution of deformation rates (a) Taiyuan City and (b) Yuncheng City.

Finally, the SAR plane coordinates were projected to the WGS-84 coordinate system by geocoding, and a product output coherence threshold of 0.3 was set to obtain the InSAR deformation field in the line of sight (LOS) direction for the two cities, i.e., the spatial distribution and time series characteristics of the surface deformation rate, as shown in Figure 12.

Figure 12 shows that significant surface deformation exists in Yuncheng City and Taiyuan City, in which the annual deformation rate of Yuncheng City ranges from -227 to 106 mm/a, which is mainly based on uplift, while the deformation rate of Taiyuan City ranges from -83 to 152 mm/a, which is mainly based on subsidence. From the characteristics of spatial distribution, the change trends of the surface and GWS are more consistent. To further analyze the relationship between the two, the time series characteristics of
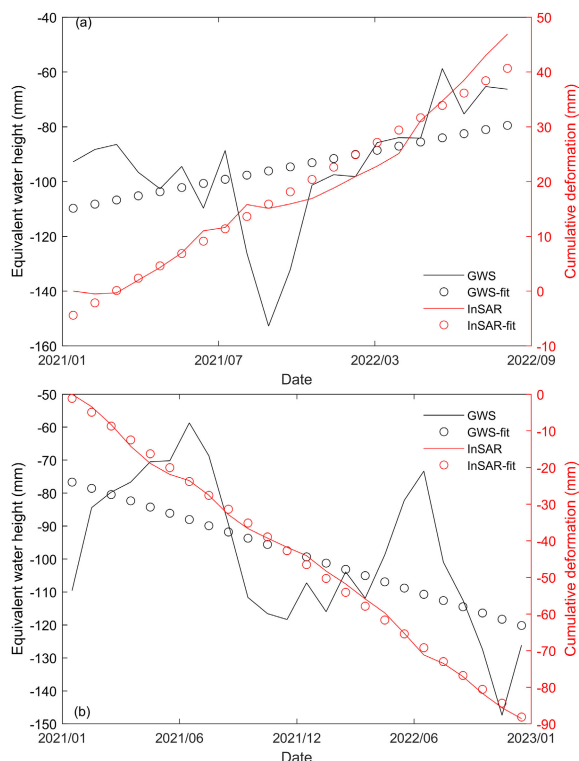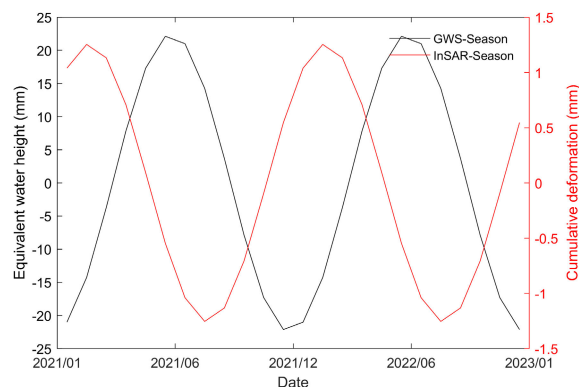
FIGURE 13. Time series characterization of GWS and surface deformation (a) Yuncheng City and (b) Taiyuan City.

FIGURE 14. Seasonal time series of groundwater and surface deformation in Taiyuan.

FIGURE 15. Original signal and decomposed signal.

GWS and surface deformation in the two places are extracted, as shown in Figure 13. It can be seen that the overall patterns of both groundwater and surface show the same trend during the period 2021-2023, with the surface in continuous uplift or decline, while the groundwater is affected by rainfall and shows seasonal changes. The strong correlation between the two indicates that groundwater changes are the main cause of surface deformation. However, deformation tends to lag behind groundwater changes due to the presence of low-permeability media in the aquifer system. Correlation analysis of seasonal time series can estimate the time at which surface deformation lags groundwater changes. As shown in Figure 14, the time series of both groundwater and surface deformation has a single-peak distribution over one year, influenced by seasonal precipitation, and the surface begins to change about 6 months after the groundwater changes. This is mainly due to the low vertical permeability coefficient of this aquifer system, and it takes a longer time for the head of the mined aquifer to reach equilibrium with the adjacent aquifer or weakly permeable layer.
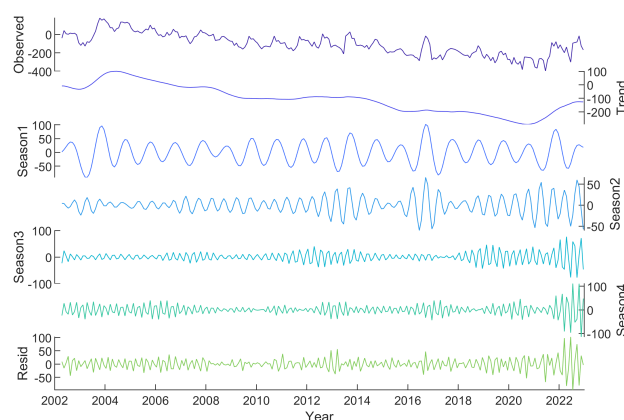
VI. PREDICTION OF GROUNDWATER STORAGE CHANGE
A. PARAMETER SETTING
The GWS data from 2002 to 2022 in the previous inversion, totaling 249 groups, were selected as the original data, of which the first 70% totaling 174 groups were used as the training set, and 69 groups out of the last 30% were used as the test set. According to the seasonal change rule, the delay step was set to 6, i.e., the first 6 months' data were used as inputs

to the model to predict the 7th-month data. Since the change of GWS is disturbed by many factors such as underground resource extraction and regional seasonal rainfall, which makes the change trend complex and diverse, it is difficult to obtain useful information from it directly. Therefore, based on the idea of signal decomposition, VMD technology is used to decompose the original signals and obtain the component signals with a certain pattern of change, and the value of modal number k is very important in the process of VMD decomposition, and improper decomposition number will cause the information of the original signals to be mixed and lost. A heuristic was used to determine the value of K. Let K increase from 2 and stop when the center frequencies of adjacent modes differ by less than 50%, at which point we observe that the corresponding center frequencies are more dispersed. In this experiment, the optimal solution is when K is equal to 5, so the original signal is decomposed into 5 modal components. As shown in Figure 15. Where IMF1 is input into the SSA-BP model as the trend term, IMF2-IMF5 is input into the SSA-LSTM model as the season term, and Resid is the residual term, which is negligible compared to the season and trend terms.

To show the optimization performance of SSA, the Whale Optimization Algorithm (WOA) is introduced to compare the ability of SSA and WOA to optimize the LSTM model, and
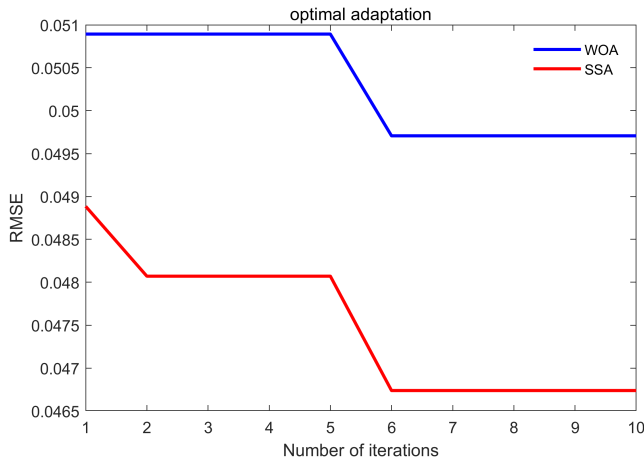
**FIGURE 16.** Evolutionary convergence curves of SSA-LSTM model and WOA-LSTM model.

their evolutionary convergence curves are shown in Figure 16, and it can be found that the optimization performance of SSA is stronger than that of WOA under the same setup parameter conditions. The three optimal hyperparameters of the LSTM model are found by SSA: the optimal number of hidden units is 51, the optimal maximum training period is 300, and the optimal initial learning rate is 0.01; and the thresholds of each neuron in the output layer and the hidden layer in the BP model, as well as the weights between the output layer and the hidden layer, are found by SSA.

B. MODEL COMPARISON AND ERROR ANALYSIS

Five prediction models, LSTM, VMD-LSTM, VMD-SSA-LSTM, BP, and SSA-BP, were constructed respectively, and the season term and trend term components of GWS were predicted. The reliability of the LSTM model after applying the signal decomposition and optimization algorithms is evaluated according to different indicators, as shown in Table 2. It can be seen that compared with the other two models, the VMD-SSA-LSTM model shows obvious advantages in both datasets, and each evaluation index is significantly improved, which indicates that the prediction accuracy of the VMD-SSA-LSTM model is better in comparison with the LSTM and VMD-LSTM models. Moreover, the values of the indicators in the training set and test set are close to each other, which indicates that there is no overfitting phenomenon in the predicted data. Figure 17 shows the comparison of the prediction results and prediction errors of the three models. It can be seen that the LSTM model predicts the largest difference between the results and the real values, and the prediction effect is average, while the VMD-SSA-LSTM model has the best overlap between the predicted and the actual values, and the prediction ability is excellent, and the VMD-LSTM model has a good prediction ability, which is in between the two. The comparison of the prediction results and the prediction errors of the BP model and the SSA-BP model is shown in Figure18, and it can be seen that the SSA-optimized BP model has
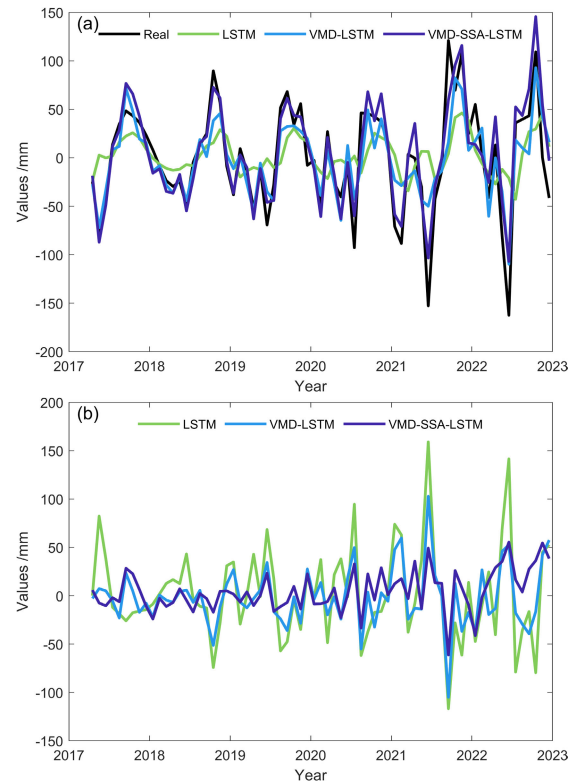
FIGURE 17. Comparison of the prediction results of the three LSTM models (a) Comparison of observed and predicted values (b) Comparison of errors.
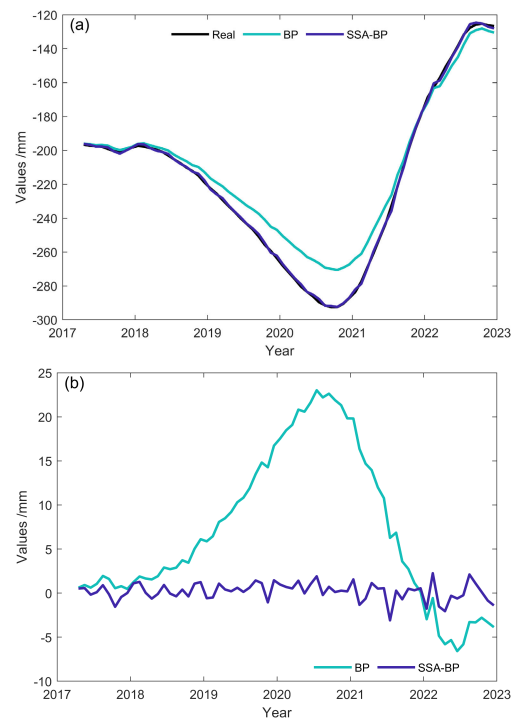
FIGURE 18. Comparison of the prediction results of the two BP models (a) Comparison of observed and predicted values (b) Comparison of errors.

higher prediction accuracy, and the predicted values almost coincide with the real values, and the prediction results are
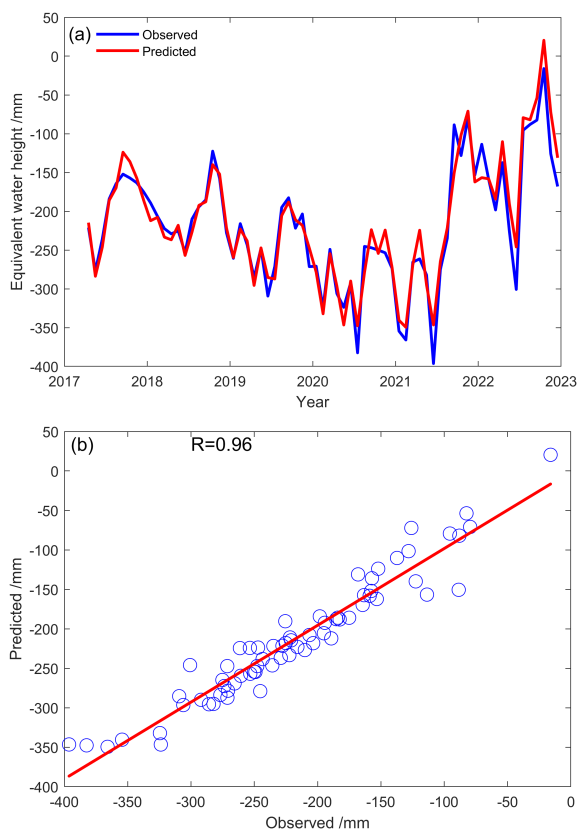
FIGURE 19. Comparison of observed and predicted values (a) Fitted curves and (b) Correlation analysis.

TABLE 2. Statistics of the results of the three models during calibration and validation phrases.

Datasets	Evaluation indicators	LSTM	VMD-LSTM	VMD-SSA-LSTM
Test	RMSE	7.55	2.20	1.56
	MAE	6.01	2.01	1.26
	MAPE/%	72.82	19.76	15.92

nearly perfect. The predicted values of the trend, period and residual terms are summed to obtain the predicted results of the original signal, as shown in Fig. 18a, Observed is the observed value of GWS and Predicted is the predicted value of GWS. The scatter plot of Figure 19b reflects the connection between the observed and predicted values of GWS, and it can be seen that the two have a strong correlation, and the Pearson correlation coefficient R is as high as 0.96, which indicates that the accuracy of the multi-source neural network prediction model based on the VMD-SSA reaches the general standard, and the model has a high degree of credibility, and it can be applied to the prediction of GWS.

Although trends in GWS are complex and vulnerable to anthropogenic activities and seasonal hydrological climate change, the prediction of GWS becomes simple and feasible after applying appropriate neural network models to different components from the idea of signal decomposition,
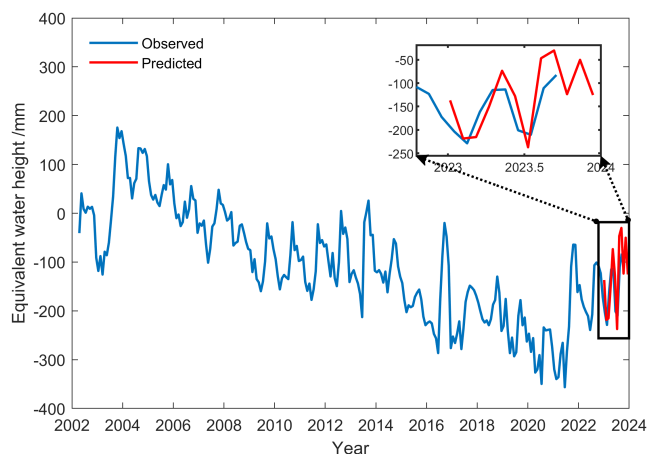

FIGURE 20. Results of prediction of changes in GWS in the coming year.

which also reflects that the prediction performance of the multi-source neural network model is better than that of the single neural network prediction model.

C. FUTURE PREDICTIONS
Predicting short-term changes in GWS can be used to assist decision-making, and prevent and mitigate problems such as groundwater depletion. It is of great significance for the comprehensive management of groundwater, the optimal allocation of water resources, and the rational development of mineral resources. Therefore, at the end of this paper, based on the last 6 months data of the existing information, i.e., the GWS data from June to December 2022, the trained network model is used to predict the change of GWS in the coming year. The predicted results are shown in Figure 20, where the predicted value of groundwater storage fluctuates cyclically over time and demonstrates an upward trend, and is compared with the latest available groundwater storage data, which are found to be relatively consistent in terms of cyclicity and trend. However, after 12 months, the predicted values show a smooth state, i.e., the GWS remains unchanged, indicating that the VMD-SSA-multi-source neural network model is suitable for short-term prediction of the GWS, and it is more appropriate to set the prediction step size within 12 months. For long-term simulation, the model may lose its effect due to the continuous accumulation of errors [50].

VII. CONCLUSION
Taking Shanxi Province as an example in this study, we used GRACE satellite gravity data to monitor groundwater changes from 2002 to 2022, and also explored the relationship between groundwater and precipitation and surface deformation. And a multi-source prediction model was developed to make time series predictions of GWS from GRACE data.

Firstly, TWS and GWS in the study area are both characterized by cyclical fluctuations in time sequence, and as a whole show a trend of change that first rises, then falls and

then rises, and changes inTWS are mainly caused by changes in GWS. GWS have been in deficit for a long time, with a deficit rate of about 1.9 mm/month, but since the second half of 2021, GWS have started to rebound due to measures such as groundwater resources control. The spatial characteristics of GWS show significant distribution differences from north to south, with annual change rates fluctuating between -21 and 4 mm/. The deficit status starts from the southeast corner of Shanxi Province and moves northwestward, with the largest deficit areas occurring in Changzhi and Jinzhong cities.

Moreover, the interannual and seasonal variation characteristics of GWS changes in Shanxi Province are closely related to the local precipitation anomaly and seasonal rainfall, with relatively high precipitation in the south driving the growth of groundwater storage in the southern region. GWS and precipitation trends are positively correlated, with GWS declining sharply when precipitation is lower than average, and rebounding when precipitation anomalies are positive. GWS shows a decreasing trend in the spring and fall, and a significant increasing trend in the summer and winter.

Furthermore, focusing on the extraction of surface deformation in cities with significant changes in GWS, it is found that surface deformation is greatly influenced by changes in GWS, and their spatial distribution has good consistency, with some correlation and lag in the time series changes. Due to seasonal precipitation, the time series of both groundwater and surface deformation shows a single-peak distribution within a year, and the surface deformation of Taiyuan City lags behind the groundwater changes by about 6 months.

Finally, the RMSE, MAE, and MAPE of the LSTM/BP prediction model after VMD decomposition and SSA optimization are reduced, and it can also be seen from the fitting curves that theVMD-SSA-LSTM/BP model can better capture the cyclical and trending fluctuation changes of the time-series data, and minimize the errors between the observed values and the predicted values. Through the correlation analysis, the Pearson correlation coefficient between the observed and predicted values is as high as 0.96, and the prediction results for the next 12 months are basically in agreement with the actual values, which indicates that the accuracy of the prediction model is very good and is suitable for predicting the short-term changes in GWS.

There are still many shortcomings in the current work, and future research directions should include two aspects. On the one hand, the inversion accuracy of GWS should be further improved to provide a more accurate data source for the prediction stage. On the other hand, the study of the correlation between groundwater and surface deformation should be deepened, the elastic skeleton storage coefficient of the aquifer system should be estimated, and the response of the aquifer system to changes in groundwater should be studied.

CONFLICTS OF INTEREST

The authors declare no conflict of interest.

REFERENCES

[1] Y. Wada, D. Wisser, and M. F. P. Bierkens, "Global modeling of withdrawal, allocation and consumptive use of surface water and groundwater resources," *Earth Syst. Dyn.*, vol. 5, no. 1, pp. 15–40, Jan. 2014, doi: 10.5194/esd-5-15-2014.

[2] T. C. McStraw, S. T. Pulla, N. L. Jones, G. P. Williams, C. H. David, J. E. Nelson, and D. P. Ames, "An open-source web application for regional analysis of GRACE groundwater data and engaging stakeholders in groundwater management," *JAWRA J. Amer. Water Resour. Assoc.*, vol. 58, no. 6, pp. 1002–1016, Dec. 2022, doi: 10.1111/1752-1688.12968.

[3] J. S. Famiglietti, "The global groundwater crisis," *Nature Climate Change*, vol. 4, no. 11, pp. 945–948, Nov. 2014, doi: 10.1038/nclimate2425.

[4] R. G. Taylor et al., "Ground water and climate change," *Nature Climate Change*, vol. 3, no. 4, pp. 322–329, Apr. 2013, doi: 10.1038/nclimate1744.

[5] A. J. Purdy, C. H. David, M. S. Sikder, J. T. Reager, H. A. Chandanpurkar, N. L. Jones, and M. A. Matin, "An open-source tool to facilitate the processing of GRACE observations and GLDAS outputs: An evaluation in Bangladesh," *Frontiers Environ. Sci.*, vol. 7, p. 155, Oct. 2019, doi: 10.3389/fenvs.2019.00155.

[6] W. Li, "Monitoring groundwater storage variations in the Guanzhong area using GRACE satellite gravity data," *Chin. J. Geophys.*, vol. 61, no. 6, pp. 2237–2245, 2018, doi: 10.6038/cjg2018L0445.

[7] G. Strassberg, B. R. Scanlon, and M. Rodell, "Comparison of seasonal terrestrial water storage variations from GRACE with groundwater-level measurements from the high plains aquifer (USA)," *Geophys. Res. Lett.*, vol. 34, no. 14, Jul. 2007, Art. no. L14402, doi: 10.1029/2007gl030139.

[8] A. Arshad, A. Mirchi, M. Samimi, and B. Ahmad, "Combining downscaled-GRACE data with SWAT to improve the estimation of groundwater storage and depletion variations in the irrigated Indus basin (IIB)," *Sci. Total Environ.*, vol. 838, Sep. 2022, Art. no. 156044, doi: 10.1016/j.scitotenv.2022.156044.

[9] B. D. Tapley, S. Bettadpur, J. C. Ries, P. F. Thompson, and M. M. Watkins, "GRACE measurements of mass variability in the Earth system," *Science*, vol. 305, no. 5683, pp. 503–505, Jul. 2004, doi: 10.1126/science.1099192.

[10] M. Rodell and J. S. Famiglietti, "An analysis of terrestrial water storage variations in Illinois with implications for the gravity recovery and climate experiment (GRACE)," *Water Resour. Res.*, vol. 37, no. 5, pp. 1327–1339, May 2001, doi: 10.1029/2000wr900306.

[11] M. Shamsudduha, R. G. Taylor, and L. Longuevergne, "Monitoring groundwater storage changes in the highly seasonal humid tropics: Validation of GRACE measurements in the Bengal basin," *Water Resour. Res.*, vol. 48, 2012, Art. no. W02508, doi: 10.1029/2011WR010993.

[12] M. Rodell, P. R. Houser, U. Jambor, J. Gottschalck, K. Mitchell, C.-J. Meng, K. Arsenault, B. Cosgrove, J. Radakovich, M. Bosilovich, J. K. Entin, J. P. Walker, D. Lohmann, and D. Toll, "The global land data assimilation system," *Bull. Amer. Meteorol. Soc.*, vol. 85, no. 3, pp. 381–394, Mar. 2004, doi: 10.1175/bams-85-3-381.

[13] W. Feng, "GRAMAT: A comprehensive MATLAB toolbox for estimating global mass variations from GRACE satellite data," *Earth Sci. Informat.*, vol. 12, no. 3, pp. 389–404, Sep. 2019, doi: 10.1007/s12145-018-0368-0.

[14] H. Chen, W. Zhang, N. Nie, and Y. Guo, "Long-term groundwater storage variations estimated in the Songhua River Basin by using GRACE products, land surface models, and in-situ observations," *Sci. Total Environ.*, vol. 649, pp. 372–387, Feb. 2019, doi: 10.1016/j.scitotenv.2018.08.352.

[15] Y. Xu, H. Gong, B. Chen, Q. Zhang, and Z. Li, "Long-term and seasonal variation in groundwater storage in the North China plain based on GRACE," *Int. J. Appl. Earth Observ. Geoinf.*, vol. 104, Dec. 2021, Art. no. 102560, doi: 10.1016/j.jag.2021.102560.

[16] B. F. Thomas and J. S. Famiglietti, "Identifying climate-induced groundwater depletion in GRACE observations," *Sci. Rep.*, vol. 9, no. 1, p. 4124, Mar. 2019, doi: 10.1038/s41598-019-40155-y.

[17] B. F. Thomas, J. S. Famiglietti, F. W. Landerer, D. N. Wiese, N. P. Molotch, and D. F. Argus, "GRACE groundwater drought index: Evaluation of California central valley groundwater drought," *Remote Sens. Environ.*, vol. 198, pp. 384–392, Sep. 2017, doi: 10.1016/j.rse.2017.06.026.

[18] W. Yu, H. Gong, B. Chen, C. Zhou, and Q. Zhang, "Combined GRACE and MT-InSAR to assess the relationship between groundwater storage change and land subsidence in the Beijing–Tianjin–Hebei region," *Remote Sens.*, vol. 13, no. 18, p. 3773, Sep. 2021, doi: 10.3390/rs13183773.

[19] P. Castellazzi, L. Longuevergne, R. Martel, A. Rivera, C. Brouard, and E. Chaussard, "Quantitative mapping of groundwater depletion at the water management scale using a combined GRACE/InSAR approach," *Remote Sens. Environ.*, vol. 205, pp. 408–418, Feb. 2018, doi: 10.1016/j.rse.2017.11.025.

[20] A. Rateb and C.-Y. Kuo, "Quantifying vertical deformation in the Tigris–Euphrates basin due to the groundwater abstraction: Insights from GRACE and Sentinel-1 satellites," *Water*, vol. 11, no. 8, p. 1658, Aug. 2019, doi: 10.3390/w11081658.

[21] J. A. Reeves, R. Knight, H. A. Zebker, P. K. Kitanidis, and W. A. Schreüder, "Estimating temporal changes in hydraulic head using InSAR data in the San Luis Valley, Colorado," *Water Resour. Res.*, vol. 50, no. 5, pp. 4459–4473, May 2014, doi: 10.1002/2013wr014938.

[22] J. A. Reeves, R. Knight, H. A. Zebker, W. A. Schreüder, P. S. Agram, and T. R. Lauknes, "High quality InSAR data linked to seasonal change in hydraulic head for an agricultural area in the San Luis Valley, Colorado," *Water Resour. Res.*, vol. 47, no. 12, p. 2010, Dec. 2011, Art. no. 2010WR010312, doi: 10.1029/2010wr010312.

[23] J. Chen, R. Knight, H. A. Zebker, and W. A. Schreüder, "Confined aquifer head measurements and storage properties in the San Luis Valley, Colorado, from spaceborne InSAR observations," *Water Resour. Res.*, vol. 52, no. 5, pp. 3623–3636, May 2016, doi: 10.1002/2015wr018466.

[24] M. Li, J. Sun, L. Xue, Z. Shen, B. Zhao, and L. Hu, "Characterization of aquifer system and groundwater storage change due to South-to-North water diversion project at Huairou groundwater reserve site, Beijing, China, using geodetic and hydrological data," *Remote Sens.*, vol. 14, no. 15, p. 3549, Jul. 2022, doi: 10.3390/rs14153549.

[25] Y. Ping, W. Xinmin, and L. Laijun, "Predicting the trends of pollutant concentrations in groundwater based on the combined method of the improved quantification theory and RBF artificial neural network," *Earth Sci. Frontiers*, vol. 23, no. 3, p. 151, May 2016, doi: 10.13745/j.esf.2016.03.019.

[26] J. Wang, L. Yang, Y. Chen, and Y. Shen, "Prediction of watershed groundwater storage based on seasonal adjustment and NAR neural network," *Geomatics Inf. Sci. Wuhan Univ.*, vol. 47, no. 10, pp. 1796–1804, 2022, doi: 10.13203/j.whugis20210584.

[27] Z. Sun, D. Long, W. Yang, X. Li, and Y. Pan, "Reconstruction of GRACE data on changes in total water storage over the global land surface and 60 basins," *Water Resour. Res.*, vol. 56, no. 4, 2020, Art. no. e2019WR026250, doi: 10.1029/2019WR026250.

[28] P. Malakar, A. Mukherjee, S. N. Bhanja, R. K. Ray, S. Sarkar, and A. Zahid, "Machine-learning-based regional-scale groundwater level prediction using GRACE," *Hydrogeol. J.*, vol. 29, no. 3, pp. 1027–1042, May 2021, doi: 10.1007/s10040-021-02306-2.

[29] A. Wunsch, T. Liesch, and S. Broda, "Forecasting groundwater levels using nonlinear autoregressive networks with exogenous input (NARX)," *J. Hydrol.*, vol. 567, pp. 743–758, Dec. 2018, doi: 10.1016/j.jhydrol.2018.01.045.

[30] S. Yi and N. Sneeuw, "Filling the data gaps within GRACE missions using singular spectrum analysis," *J. Geophys. Res., Solid Earth*, vol. 126, no. 5, 2021, Art. no. e2020JB021227, doi: 10.1029/2020JB021227.

[31] F. G. Dai, F. W. Zhang, B. Wang, Z. T. Han, and B. W. Hu, "Changes of the groundwater flow field of Lu'an mining area, Shanxi Province, under the condition of group mining," *Acta Geoscientica Sinica*, vol. 39, no. 1, pp. 94–102, 2018, doi: 10.3975/cagsb.2017.122002.

[32] X. Chen, J. Jiang, T. Lei, and C. Yue, "GRACE satellite monitoring and driving factors analysis of groundwater storage under high-intensity coal mining conditions: A case study of Ordos, northern Shaanxi and Shanxi, China," *Hydrogeol. J.*, vol. 28, no. 2, pp. 673–686, Mar. 2020, doi: 10.1007/s10040-019-02101-0.

[33] J. Wahr, M. Molenaar, and F. Bryan, "Time variability of the Earth's gravity field: Hydrological and oceanic effects and their possible detection using GRACE," *J. Geophys. Res., Solid Earth*, vol. 103, no. B12, pp. 30205–30229, Dec. 1998, doi: 10.1029/98jb02844.

[34] D. Chen, X. Zeng, J. Wu, D. Gui, and Y. Sun, "Study on the evolution of groundwater storage variations in the Tarim river basin based on GRACE and GLDAS," *Geological J. China Universities*, vol. 28, no. 6, pp. 894–901, 2022, doi: 10.16108/j.issn1006-7493.2021012.

[35] J. Zhu, Z. Li, and J. Hu, "Research progress and methods of InSAR for deformation monitoring," *Acta Geodaetica Cartographica Sinica*, vol. 46, no. 10, p. 1717, Oct. 2017, doi: 10.11947/j.AGCS.2017.20170350.

[36] T. G. Farr, P. A. Rosen, E. Caro, R. Crippen, R. Duren, S. Hensley, M. Kobrick, M. Paller, E. Rodriguez, L. Roth, D. Seal, S. Shaffer, J. Shimada, J. Umland, M. Werner, M. Oskin, D. Burbank, and D. Alsdorf, "The shuttle radar topography mission," *Rev. Geophys.*, vol. 45, no. 2, p. 361, Jun. 2007, doi: 10.1029/2005rg000183.

[37] Y. Lu, H. Yan, J. Yang, and X. Duan, "Analysis of the effect of different resolution DEM on InSAR deformation monitoring accuracy," *J. Geomatics*, vol. 43, no. 6, pp. 106–109, 2018, doi: 10.14188/j.2095-6045.2016444.

[38] P. Berardino, G. Fornaro, R. Lanari, and E. Sansosti, "A new algorithm for surface deformation monitoring based on small baseline differential SAR interferograms," *IEEE Trans. Geosci. Remote Sens.*, vol. 40, no. 11, pp. 2375–2383, Nov. 2002, doi: 10.1109/TGRS.2002.803792.

[39] R. Lanari, O. Mora, M. Manunta, J. J. Mallorqui, P. Berardino, and E. Sansosti, "A small-baseline approach for investigating deformations on full-resolution differential SAR interferograms," *IEEE Trans. Geosci. Remote Sens.*, vol. 42, no. 7, pp. 1377–1386, Jul. 2004, doi: 10.1109/tgrs.2004.828196.

[40] F. Casu, M. Manzo, and R. Lanari, "A quantitative assessment of the SBAS algorithm performance for surface deformation retrieval from DInSAR data," *Remote Sens. Environ.*, vol. 102, nos. 3–4, pp. 195–210, Jun. 2006, doi: 10.1016/j.rse.2006.01.023.

[41] K. Dragomiretskiy and D. Zosso, "Variational mode decomposition," *IEEE Trans. Signal Process.*, vol. 62, no. 3, pp. 531–544, Feb. 2014, doi: 10.1109/TSP.2013.2288675.

[42] J. Xue and B. Shen, "A novel swarm intelligence optimization approach: Sparrow search algorithm," *Syst. Sci. Control Eng.*, vol. 8, no. 1, pp. 22–34, Jan. 2020, doi: 10.1080/21642583.2019.1708830.

[43] S. Hochreiter and J. Schmidhuber, "Long short-term memory," *Neural Comput.*, vol. 9, no. 8, pp. 1735–1780, Nov. 1997, doi: 10.1162/neco.1997.9.8.1735.

[44] J. Schmidhuber, "Deep learning in neural networks: An overview," *Neural Netw.*, vol. 61, pp. 85–117, Jan. 2015, doi: 10.1016/j.neunet.2014.09.003.

[45] S. Li, P. Shuai, X. Gu, X. Fu, S. Ni, and N. Zhang, "GRACE-based monitoring groundwater change in coal mining areas," *J. Hydraulic Eng.*, vol. 52, no. 12, pp. 1439–1448, 2021, doi: 10.13243/j.cnki.slxb.20210076.

[46] D. Jin, Z. Zhou, C. Zhao, L. Feng, and F. Xu, "Dynamics process analysis of groundwater quantity loss of roof aquifer with shallow seam mining in Western China," *J. China Coal Soc.*, vol. 44, no. 3, pp. 690–700, 2019, doi: 10.13225/j.cnki.jccs.2018.6033.

[47] Z. Tao, T. Tao, X. Ding, and R. He, "Groundwater storage changes in Anhui province derived from GRACE and GLDAS hydrological model," *Prog. Geophys.*, vol. 36, no. 4, pp. 1456–1463, 2021.

[48] Y. An and F. Yan, "InSAR monitoring and inversion of fault slip distribution for the 2021 Yunnan Yangbi earthquake," *J. Geodesy Geodyn.*, vol. 43, no. 5, pp. 509–516, 2021, doi: 10.14075/j.jgg.2023.05.013.

[49] F. Yang, Y. An, C. Ren, J. Xu, J. Li, D. Li, and Z. Peng, "Monitoring and analysis of surface deformation in Alpine Valley areas based on multidimensional InSAR technology," *Sci. Rep.*, vol. 13, no. 1, p. 12896, Aug. 2023, doi: 10.1038/s41598-023-39677-3.

[50] Y. Chen, Y. He, L. Zhang, Y. Chen, H. Pu, B. Chen, and L. Gao, "Prediction of InSAR deformation time-series using a long short-term memory neural network," *Int. J. Remote Sens.*, vol. 42, no. 18, pp. 6919–6942, Sep. 2021, doi: 10.1080/01431161.2021.1947540.

YAN AN received the B.Eng. degree in surveying engineering from Liaoning Technical University, Fuxin, China, in 2021, where he is currently pursuing the M.S. degree.

His current research interests include geodesy and deformation monitoring, homeland space and disaster monitoring, remote sensing data processing, and InSAR monitoring.

CHUANG REN received the B.Eng. degree in surveying engineering from Liaoning Technical University, Fuxin, China, in 2021, where he is currently pursuing the M.S. degree.

FAN YANG received the B.Eng. degree from Henan Polytechnic University, Jiaozuo, China, in 1996, and the M.Eng. and Ph.D. degrees from Liaoning Technical University, Fuxin, China, in 2002 and 2006, respectively.

He is currently a Professor with the School of Geomatics, Liaoning Technical University. He is the author of three books and more than 80 articles. His current research interests include geodesy and deformation monitoring, homeland space and disaster monitoring, remote sensing data processing, and InSAR monitoring.

JIN HU received the B.Eng. degree in surveying engineering from Shanxi Institute of Technology, Yangquan, China, in 2018, and the M.S. degree in surveying engineering from Liaoning Technical University, Fuxin, China.

JIA XU received the B.Eng. degree from Northeastern University, Shenyang, China, in 2002, and the M.Eng. and Ph.D. degrees from Liaoning Technical University, Fuxin, China, in 2005 and 2010, respectively.

She is currently an Associate Professor with the School of Geomatics, Liaoning Technical University. She is the author of one book and more than five articles.

GUONA LUO received the B.Eng. degree from Yunnan Agricultural University, Kunming, China, in 2013, and the M.Eng. degree from Kunming University of Science and Technology, Kunming, in 2018.

She is currently a Tutor with the College of Hydraulic and Architectural Engineering, Tarim University. She is the author of five books and more than 15 articles. Her current research interests include territorial spatial planning and ecological restoration.

• • •